Biosensors and Bioelectronics 141 (2019) 111421

Contents lists available at ScienceDirect

Biosensors and Bioelectronics

journal homepage: www.elsevier.com/locate/bios

Atomic matching catalysis to realize a highly selective and sensitive biomimetic uric acid sensor

Zhuanzhuan Shi[a,1], Xiaoli Li[c,1], Ling Yu[b], Xiaoshuai Wu[a], Jinggao Wu[b], Chunxian Guo[a,**], Chang Ming Li[a,b,d,*]

[a] Institute of Materials Science and Devices, Suzhou University of Science and Technology, Suzhou, 215011, China
[b] Institute for Clean Energy and Advanced Materials, School of Materials and Energy, Southwest University, Chongqing, 400715, China
[c] College of Biosystems Engineering and Food Science, Zhejiang University, Hangzhou, 310058, China
[d] Institute of Advanced Cross-field Science, College of Life Science, Qingdao University, Qingdao, 266071, China

ARTICLE INFO

Keywords:
Biomimetic enzyme
Biosensor
Atomic matching catalysis
Uric acid detection
High selectivity

ABSTRACT

A main challenge for biomimetic non-enzyme biosensors is to achieve high selectivity. Herein, an innovative biomimetic non-enzyme sensor for electrochemical detection of uric acid (UA) with high selectivity and sensitivity is realized by growing Prussian blue (PB) nanoparticles on nitrogen-doped carbon nanotubes (N-doped CNTs). The enhancement mechanism of the biomimetic UA sensor is proposed to be atomically matched active sites between two reaction sites (oxygen atoms of 2, 8-trione, 6.9 Å) of UA molecule and two redox centers (Fe^{II} on the diagonal, 7.2 Å) of PB. Such an atomically matching manner not only promotes strong adsorption of UA on PB but also selectively enhances electron transfer between reaction sites of UA and active Fe^{II} centers of PB. This biomimetic UA sensor can offer great selectivity to avoid interferences from other oxidative and reductive species, showing excellent selectivity. An electrochemical biomimetic sensor based on PB/N-doped CNTs was applied to *in situ* detect UA in human serum, delivering a wide dynamic detection range (0.001–1 mM) and a low detection limit (0.26 μM). This work provides a high-performance UA sensor while shedding a scientific light on using atomic matching catalysis to fabricate highly sensitive and selective biomimetic sensors.

1. Introduction

Uric acid (UA) is the main end-product of human purine metabolism, and plays an irreplaceable role in important physiological processes (Martinon, 2010). The normal UA levels in human serum is in a range of 0.09–0.42 μM (Ghosh et al., 2015). Abnormal UA concentrations can cause disorders in purine metabolism, which can lead to fatal diseases like gout, hyperuricemia, Lesch-Nyhan syndrome, leukemia, pneumonia (Bishop and Talbott, 1953), cardiovascular disease, oxidative stress and multiple sclerosis (Martinon, 2010). Currently, detection of UA levels is mainly conducted in clinical practices by enzymatic methods (Liu et al. 2016, 2017a; Tiwari et al., 2016), fluorescence (Liu et al., 2017b), high-performance liquid chromatography (Krstulovic et al., 1977), chemiluminescence (Yu et al., 2011) and electrochemical (Liao et al., 2015) techniques. Among these methods, electrochemical detections can offer advantages of simplicity, fast detection, remarkable sensitivity and specificity, while favoring to point-of-care testing (POCT) (Choi et al., 2010; Lang et al., 2013; Li et al., 2015b; Shi et al., 2019). However, electrochemical UA sensors always rely on enzyme uricase, an oxidase that oxidizes UA to produce hydrogen peroxide (H_2O_2), which is subsequently electrochemically detected by peroxidase or nanomaterials (Tiwari et al., 2016). An enzyme-based sensor is complicated and often suffers from the high enzyme expense, short shelf-life, poor stability and easy loss enzyme activity. Additionally, the fabrication of enzyme-based UA sensors is very tedious (Lee et al., 2016; Noh and Park, 2018). Thus, biomimetic sensors without the use of uricase can overcome the shortcomings of the enzyme-based ones and thus are highly desired.

Nanomaterials have been explored as biomimetic enzyme for UA detection (Guo et al., 2012; Hu et al., 2015; Li et al., 2015a; Ma et al., 2014). For example, nitrogen (N)-doped carbon materials have been used for UA detection, in which pyridine-like N component is responsible for the electrocatalytic activity in the oxidation of UA (Sheng et al., 2012). Unfortunately, such sensors face great challenges not only

* Corresponding author. Institute of Materials Science and Devices, Suzhou University of Science and Technology, Suzhou, 215011, China.
** Corresponding author. Institute of Materials Science and Devices, Suzhou University of Science and Technology, Suzhou, 215011, China.
E-mail address: ecmli@swu.edu.cn (C.M. Li).
[1] Equal contribution.

https://doi.org/10.1016/j.bios.2019.111421
Received 19 February 2019; Received in revised form 21 May 2019; Accepted 6 June 2019
Available online 07 June 2019
0956-5663/

from low sensitivity, but also from the poor selectivity without the enzyme as a catalyst. In particular, UA detection has strong interferences since some biological species like ascorbic acid (AA) and dopamine (DA) have similar oxidation potential windows as UA for extremely poor selectivity. Therefore, design and fabricate biomimetic UA sensor to achieve high selectivity is essential.

Prussian blue (PB) have been used as a biomimetic peroxidase in our lab and other groups for electrochemical sensing H_2O_2 with both oxidation and reduction manners. For electrochemical reduction of H_2O_2, the cathodic peak of PB responses to the PB-to-Prussian white (PW) conversion, followed by electrochemical reduction of H_2O_2. PW is believed to have the active sites for electrochemical reduction of H_2O_2 (Guo et al., 2010). Inspiring from enzyme catalytic mechanism, the key factor to essentially improve the selectivity of a biomimetic UA sensor is to create enzyme-like redox center that can perfectly match the reaction site of UA to actually realize an atomic matching catalysis. It is expected that PB with a rational design might enable an atomic matching catalysis for highly selective and sensitive detection of UA. However, such a possibility has never been explored yet. In this work, an innovative biomimetic enzyme comprising PB nanoparticles on nitrogen-doped carbon nanotubes (N-doped CNTs) is designed (Scheme S1), and for the first time used to electrochemically detect UA. Surprisingly, the sensor demonstrates high selectivity and sensitivity. Interaction of PB/N-doped CNTs and UA molecules was investigated by theoretical calculation. The catalytic process of electrochemical detection of UA molecules on the PB/N-doped CNTs was explored and discussed. Accordingly, atomic marching catalysis mechanism of the PB/N-doped CNTs for the biomimetic sensing of UA is proposed. A flexible screen-printed electrode (SPE) based on the PB/N-doped CNTs was used to construct UA detection platform, achieving *in-situ* UA detection in human serum with high sensitivity and selectively.

2. Materials and methods

2.1. Materials

Carbon ink (BQ 221) was purchased from Du Pont (USA). CNTs, ammonium persulfate (APS), UA, AA, DA, glucose, 30% H_2O_2 were all purchased from Sigma Aldrich. PBS, aniline (ANI), Iron (III) chloride hexahydrate ($FeCl_3.6H_2O$), potassium ferricyanide [$K_3Fe(CN)_6$], sulfuric acid (H_2SO_4), nitric acid (HNO_3), perchloric acid ($HClO_4$), hydrochloric acid (HCl), Nafion were purchased from Chongqing Co. Human serum was purchased from Gibco (USA). All other chemicals used in this study were analytical grade. The deionized water used in all experiments is produced by Q-Grad®1 system, Millipore Corporation.

2.2. Synthesis of PB/N-doped CNTs

Firstly, CNTs was treated with acid (H_2SO_4, HNO_3) as previously reported (Tian et al., 2014). Next, the acid-treated CNTs was re-suspended in 1 M $HClO_4$ by ultrasonic dispersion and stirred in an ice bath for 30 min. Then ANI (1 mM, dispersed in 1 M $HClO_4$) was added to the prepared CNTs dispersion at a stable flow rate (0.05 mL/min). Next, APS (1 mM, dissolved in 1 M $HClO_4$) was added into this dispersion at a flow rate of 0.025 mL/min and kept stirring in an ice bath for 6 h to form polyaniline/CNTs (PANI/CNTs). The N-doped CNTs powder was obtained by carbonizing freeze-dried PANI/CNTs under an argon atmosphere at 900 °C for 2 h. For synthesis of PB/N-doped CNTs, an acidic solution (pH 1.5, adjusted with HCl) that contained a precise amount of $FeCl_3$ and K_3 [$Fe(CN)_6$] was added into an N-doped CNTs suspension and then reacted for 10 h under stirring.

2.3. Preparation of non-enzymatic UA strip

A two-electrode electrochemical sensor was designed by CorelDraw software (Corel, Canada). The gap between work electrode (WE) and reference/counter electrode was 0.5 mm. The diameter of the WE was 1.5 mm and the reference/counter electrode was fabricated with one order magnitude larger than the working electrode. Therefore, the polarization at the counter/reference electrode is insignificant to offer accurate measurements (Fig. S4). The electrochemical biochip was fabricated by screen-printing technology. In brief, carbon paste was printed on a plastic membrane. After printing, the biochip was heated at 110 °C for 5 min. For modifying of the SPE, 2 μL of PB/N-doped CNTs solution (2 mg/mL) was carefully drop-casted onto the WE and then 0.5 μL of 0.1 wt% Nafion was pipetted onto the PB/N-doped CNTs modified WE.

2.4. Apparatus and characterizations

The electrochemical measurements were performed on a CHI 760 E electrochemical work station (Shanghai, China). PBS (0.01 M) was used as the electrolyte for all of the electrochemical measures except in detection with human serum. The morphologies of the synthesized materials were observed by field emitted scanning electron microscopy (FESEM, JSM-7800 F) and transmission electron microscopy (TEM, JEM-2100, Japan). The surface properties of the materials were characterized by X-ray photoelectron spectroscopy (XPS, Thermo, USA). The chemical groups of the samples were recorded by Fourier transform infrared spectroscopy (FTIR, Thermo-Nicolet 6700, Japan) with air as a reference. A resolution of 4 cm^{-1} and 32 scans were applied. The crystal structure of the PB/N-doped CNTs was characterized by X-ray diffraction (XRD, MAXima-X XRD-7000).

2.5. Detection of UA in human serum

The PB/N-doped CNTs/SPE strip was applied to detect UA-spiked serum in order to investigate the practical performance of the developed UA strip. The UA-spiked serum samples were prepared by standard addition method. In brief, different concentrations of UA (200, 400, 600 μM) were spiked into the raw serum. The recovery rates were calculated based on the added concentration and the detected concentration. All experiments were repeated three times.

2.6. Stability of the non-enzymatic UA strip

The long-term storage and stability of the fabricated non-enzymatic UA strip was measured over 5 months. The prepared electrochemical strips were stored in dry conditions at room temperature and the activity of the non-enzymatic UA electrochemical strip was measured every 7 days.

3. Results and discussion

3.1. Theoretical calculation for interaction between UA and PB

To explore the possibility, theoretical calculation is first used to provide better understanding for interaction between UA molecule and PB. The calculation results reveal that distance between oxygen atoms of 2, 8-trione in the UA molecule is 6.9 Å, which is close to that (7.2 Å) between two Fe atoms locating diagonally in PB lattice (Fig. 1A). Further verification by density functional theory calculations indicates that PB (111) surface interfaces the UA monolayer, which results in a non-covalent interaction (van der Waals force) (details provide in supporting information). Calculation results also confirm that PB (111) surface exposing C and N atoms with the lowest energy is thermodynamically stable (Table S1). As shown in Fig. 1B, surface adsorption energy of UA adsorbing on the diagonally located Fe^{II}, Fe^{III} in PB lattice as well as a non-matching configuration (shorten as no match) is −11.44 eV, −7.85 eV, −7.55 eV, respectively, suggesting the strongest interaction for UA molecule aligning with diagonally located two Fe^{II} atoms in PB lattice. It is thus concluded that the two oxygen atoms of

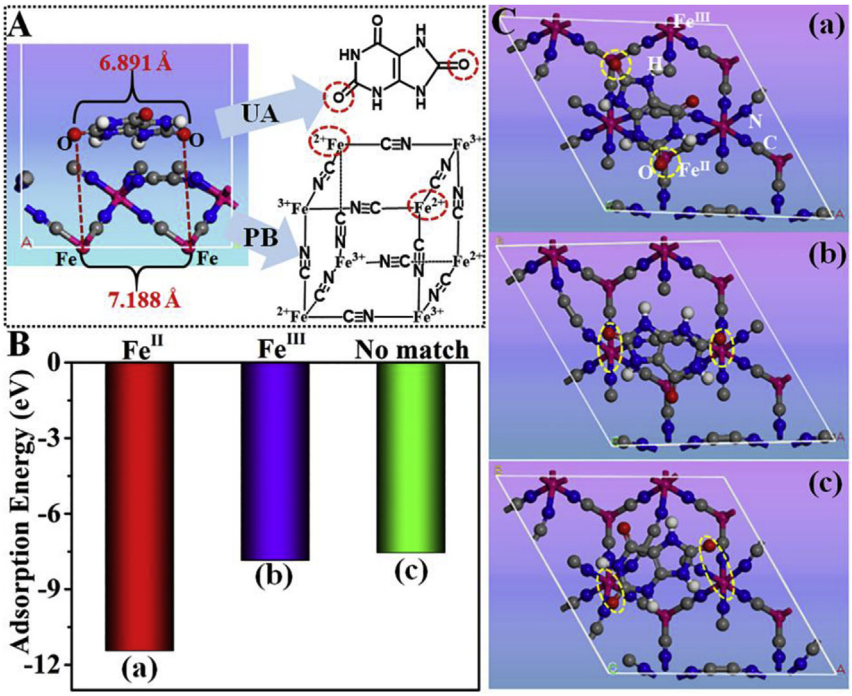

Fig. 1. A. Side view of the relaxed structure of UA molecule adsorbed on PB (111) surface. B. The calculated surface adsorption energy of a UA monolayer adsorbing on PB (111) surface: oxygen atoms of 2, 8-trione in the UA molecule matched with Fe^{II} on the diagonal in PB lattice (a), matched with Fe^{III} on the diagonal in PB lattice (b), no match (c). C. Top view of the relaxed structure of UA molecule adsorbed on PB (111) surface corresponds to B.

UA has the best match with the diagonally located two Fe^{II} atoms in comparison with that of oxygen atoms with Fe^{III} and no match (Fig. 1C). Therefore, we could infer that the strong adsorption between the oxygen atoms of UA and the two Fe^{II} atoms of PB could enable good interactions for selective electron transfer as well as for high specificity.

3.2. Characterization of synthesized PB/N-doped CNTs

The PB-based catalyst was designed and fabricated by *in-situ* depositing PB nanoparticles on N-doped CNTs (Fig. 2A). N-doped CNTs were first synthesized by carbonizing sawtooth PANI nanoarrays that was grown on CNTs with a high electrical conductivity. Then, PB nanoparticles were uniformly grown on the N-doped CNTs via chemical bath deposition method, resulting in a unique nanocomposite of PB/N-

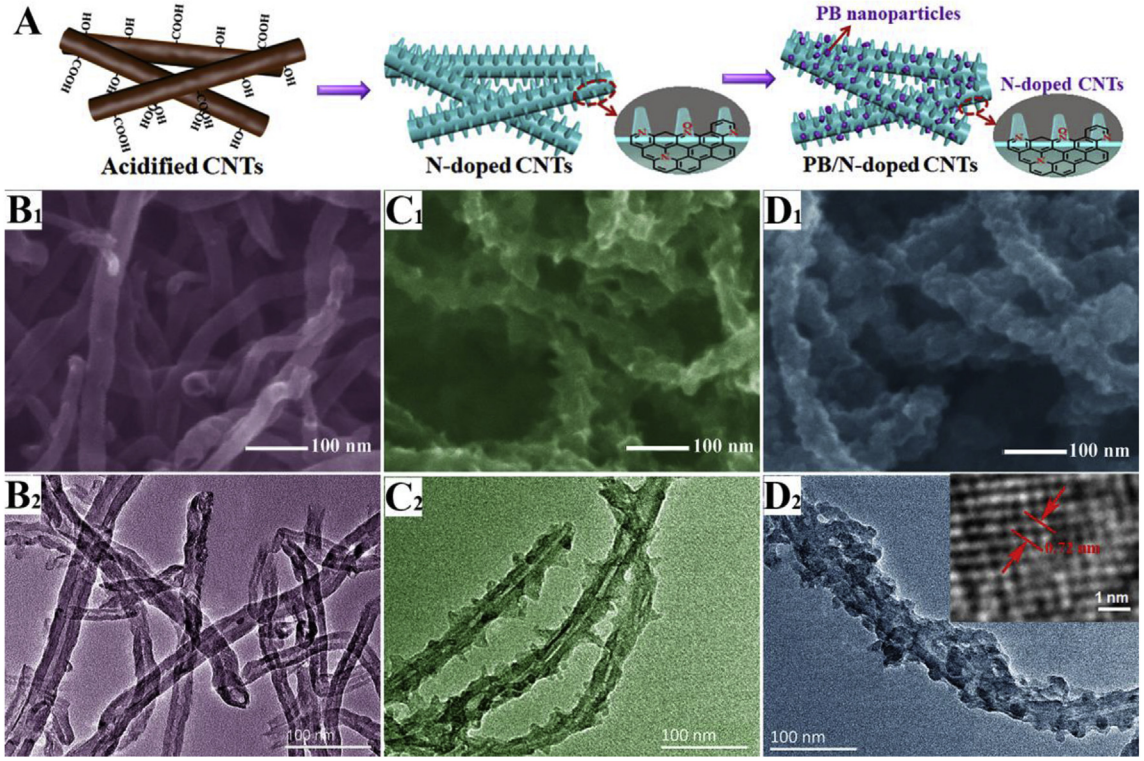

Fig. 2. A. Schematic illustration of the PB/N-doped CNTs synthesis process. B_1-D_1. FESEM images of CNTs (B_1), N-doped CNTs (C_1), and PB/N-doped CNTs (D_1). B_2-D_2. TEM images of CNTs (B_2), N-doped CNTs (C_2), and PB/N-doped CNTs (D_2). The inset of Fig. D_2 shows high resolution TEM image of PB.

doped CNTs.

Morphologies and structure of the as-fabricated PB/N-doped CNTs were investigated by FESEM and TEM (Fig. 2B_1-D_2). Deposition and subsequent carbonization of PANI form N-doped carbon in the form of sawtooth nanoarrays uniformly distributed on the CNTs (Fig. 2C_1, C_2), leading to a much rougher surface in comparison to the smooth surface of plain CNTs (Fig. 2B_1, B_2). The doping of electron-rich N atoms in the CNTs enhances the chemical stability and increases the electron density. PB nanoparticles that was synthesized using 5 mM $FeCl_3$ and $K_3Fe(CN)_6$ have an average size of around 10 nm and are uniformly anchored to surface of N-doped CNTs (Fig. 2D_1, D_2). It is found that precursor concentration of $FeCl_3$ and $K_3Fe(CN)_6$ affects the morphology and structures of PB nanoparticles on N-doped CNTs and the optimized precursor concentration is 5 mM (Fig. S2). PB nanoparticles synthesized using 2.5 mM of $FeCl_3$ and $K_3Fe(CN)_6$ have a lower loading amount and non-uniform sizes (Fig. S2A) while the size is too large when using 7.5 or even 10 mM of precursor (Figs. S2B and C). On the other hand, using the same fabrication procedures, PB nanoparticles on plain CNTs have a poorer sizes distribution and much lower loading amount, indicating that N-doping is favorable to the nucleation for uniformly growing PB nanoparticles (Fig. S2D). Furthermore, the high resolution TEM image recorded using FEI Titan Themis microscope (inset of Fig. 2D_2) shows that the Fe atoms of PB lattice fully and uniformly distributed on the surface of N-doped CNTs, which can form a strong adsorption to UA. It has been reported that pyridine and the tetravalent N atoms of N-doped carbon materials can provide high localized electron densities and surface energy differences (Wang et al., 2014). Therefore, the unique physiochemical properties of N-doped CNTs with both N doping and sawtooth structure for large surface area should be beneficial in promoting nucleation of PB nanoparticles and followed growth, eventually resulting in the uniform distribution of PB nanoparticles on N-doped CNTs with a good interfacial interaction.

Crystal structures of PB/N-doped CNTs were resolved by XRD. As shown in Fig. 3A, diffraction peaks at $2\theta = 17.54°$, 24.62°, 35.42°, 39.66°, 43.58°, 50.52°, 53.82° and 57.32° refer to (222), (220), (400), (420), (422), (440), (600) and (620) planes of PB, respectively, informing a pure face-centered-cubic phase of PB (Chen et al., 2012). Chemical attributes of the materials were investigated by XPS. Survey spectrums (Fig. S3A) confirms the presence of N doping and iron species for the PB/N-doped CNTs The main N 1s peaks at 402.5, 399.2, and 397.7 eV correspond to C–N of $[Fe(CN)_6]^{4-}$ for PB in the PB/N-doped CNTs (Fig. 3B). Fig. 3C of Fe XPS spectrum shows two characteristic peaks at 712.2 eV and 721.5 eV, which refer to the binding energies of Fe $2p_{3/2}$ and Fe $2p_{1/2}$ for the Fe^{3+} in PB. Moreover, another peak at 708.5 eV that is related to Fe $2p_{3/2}$ of $[Fe(CN)_6]^{4-}$ further proves the deposition of PB (Cao et al., 2010). Additionally, the PB on CNT is further confirmed by the FTIR spectra, in which a peak around 2066 cm^{-1} refers to the –C≡N– group in the bridge type $Fe^{2+}-C\equiv N-Fe^{3+}$ of PB (Zhang et al., 2010) (Fig. S3B). The material characterization results demonstrate successful fabrication of the nanocomposite of PB/N-doped CNTs, in which PB nanoparticles with an average size of around 10 nm are uniformly distributed on N-doped CNTs.

3.3. UA detection using the PB/N-doped CNTs-based non-enzymatic UA strip

Instead of glassy carbon electrode (GCE), SPE that is more suitable for practical applications and wearable devices was used in this work (Shi et al., 2018). The fabricated PB/N-doped CNTs-based SPE for biomimetic UA detection is shown in Fig. S4, with which electrochemical techniques including cyclic voltammetric (CV), amperometric i-t and electrochemical impedance spectroscopy (EIS) in phosphate buffered saline (PBS, pH = 7.4) containing UA were performed. As shown in Fig. 4A, the PB/N-doped CNTs in PBS solution containing UA exhibits a much larger reduction peak current than the same electrode in PBS without UA, suggesting the nature of biomimetic reductive enzyme for PB/N-doped CNTs. The reduction peak currents versus different concentrations of $FeCl_3$ and $K_3Fe(CN)_6$ that were used to fabricate PB/N-doped CNTs demonstrated that 5 mM of precursor was the optimal condition to achieve the best performance (Fig. S5). More importantly, the reduction signal of PB/N-doped CNTs is much higher than those of control samples including CNTs, N-doped CNTs and PB/CNTs. In more detailed comparison, electrodes containing PB including PB/CNTs and PB/N-doped CNTs display obvious reduction peak towards UA detection while no obvious reduction peak is observed for CNTs and N-doped CNTs, clearly evidencing that PB mainly offers the reductive catalysis towards UA. More importantly, although the N-doped CNTs electrode shows a small reduction wave toward UA reduction at very negative potential, the onset potential and half-wave potential for PB/N-doped CNTs are −0.20 and −0.37 V, which are much more positive than −0.46 and −0.58 V, respectively for N-doped CNTs (Fig. 4A). This evidently indicates that the former electrode offers much better catalytic activity than the latter because of PB immobilization. Additionally, the former delivers a peak current of 16.34 μA, which is much larger than the latter by 3 times, symbolling that the PB immobilization can also increase reaction sites than the latter by 3 times (Fig. 4A). The EIS spectra in (Fig. 4B) shows that PB/N-doped CNTs has the smallest value of charge transfer resistance (84 Ω), which is much smaller than N-doped CNTs (106 Ω), further proving that PB immobilization enable prominent catalytic effect toward UA reduction.

Electrochemical assay conditions were optimized for PB/N-doped CNTs-based UA analysis. Effect of pH on PB/N-doped CNTs/SPE was examined with a pH range of 6.5–8.5, achieving the best performance at a pH of 7.4 that is close to the biological environment (Fig. S6). All following electrochemical measurements were carried out in PBS solution with pH of 7.4. Effect of CV scan rate from 2 to 150 mV/s on

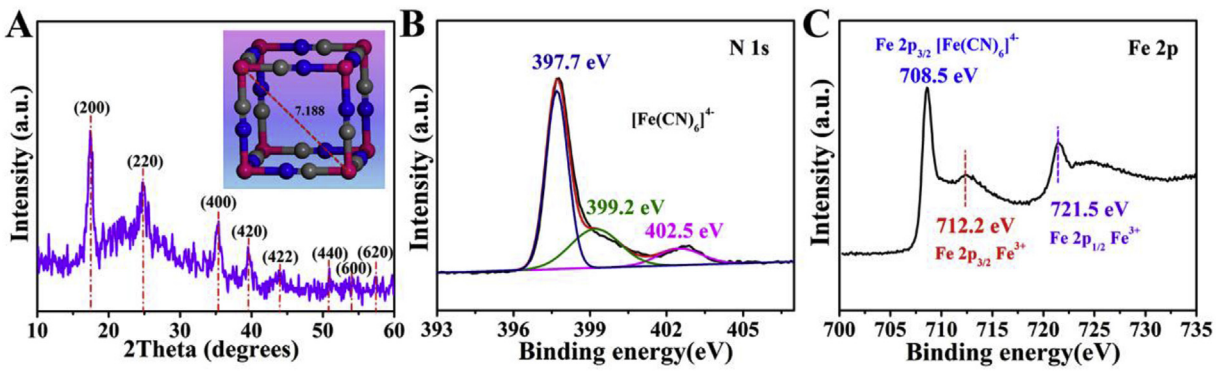

Fig. 3. A. XRD pattern of PB/N-doped CNTs nanocomposite. XPS spectra of B. N 1s spectrum in PB/N-doped CNTs nanocomposite, C. Fe 2p spectrum in PB/N-doped CNTs nanocomposite.

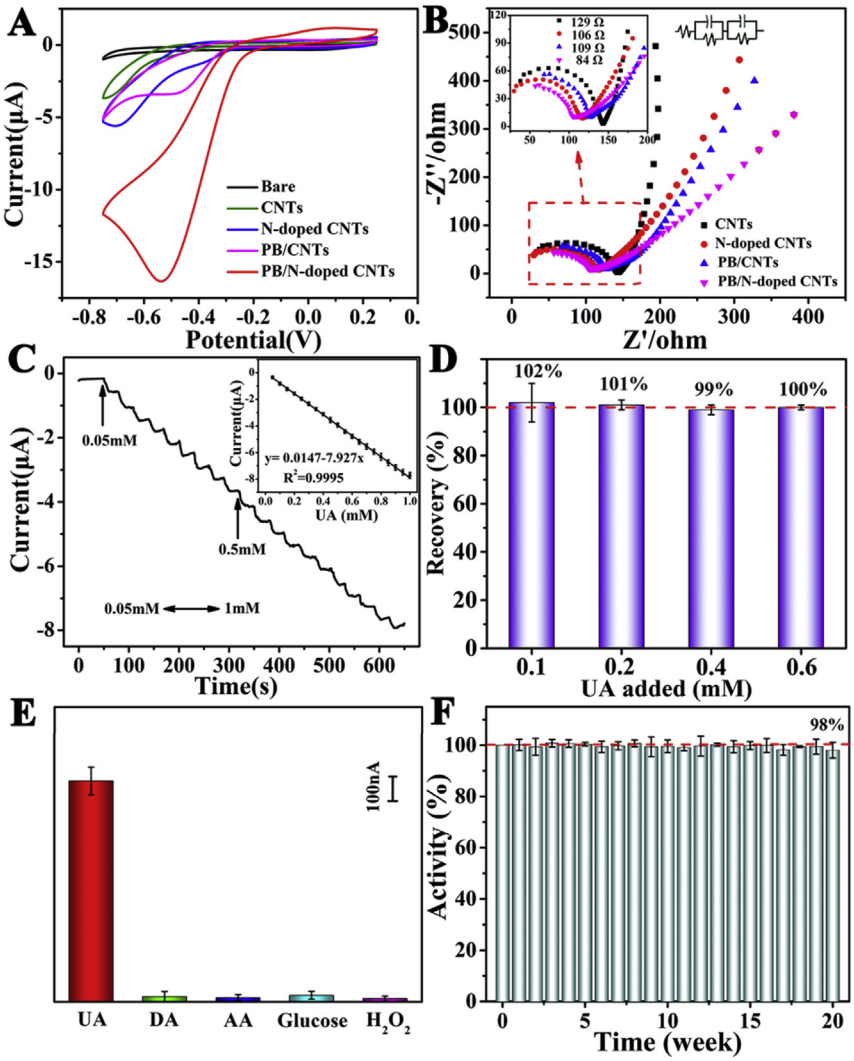

Fig. 4. A. CV curves of different materials conducted in 0.01 M PBS containing 1 mM UA, scan rate: 50 mV/s. B. EIS of different materials carried out in 0.01 M PBS between 1 and 10^6 Hz. C. I-t curve of the PB/N-doped CNTs/SPE obtained in 0.01 M PBS by adding 0.05 mM UA every 30 s at −0.5 V. The inset shows the calibration curve that calculated from three independent measurements. D. Recovery study of PB/N-doped CNTs/SPE performed by adding standard UA in human serum. E. Interference test of the fabricated PB/N-doped CNTs/SPE to different analytes (UA, DA, AA, H_2O_2: 0.2 mM, Glucose: 6 mM). F. The stability of the no-enzymatic UA strips stored at 25 °C.

catalytic behavior of the PB/N-doped CNTs/SPE was also studied (Fig. S7A). The reduction peak current was linear to the square root of scan rate, indicating a diffusion-controlled electrochemical reaction (Fig. S7B). CV responses of PB/N-doped CNTs/SPE to a series of UA concentrations were investigated (Fig. S7C). The peak current-dose responses linearly, as calculated from three independent measurements (range: 0.2–1.0 mM, y = 1.770 + 15.854*Con.[UA], R^2 = 0.998; Fig. S7D), further confirming the sensing signal from electrochemical detection of UA over the PB/N-doped CNTs/SPE.

The amperometric measurements were conducted on PB/N-doped CNTs/SPE to find out the sensitivity, detection limit and recovery ability towards UA. To achieve the best detection limit, the potential for amperometric measurement was optimized. The current-time responses of PB/N-doped CNTs/SPE to UA were recorded every 30 s by adding 0.1 mM UA at −0.45, −0.5 and −0.55 V, respectively (Fig. S8). The maximum amperometric response was achieved at a potential of −0.5 V. For real-time detection of UA, amperometric measurements were conducted by successive adding a certain concentration of UA solution over a wide range of 0.05–1 mM and at the same time, recording I-t curve at an applied potential of −0.5 V (Fig. 4C). Two concentration ranges of UA of 1–10 μM and 10–100 μM were tested to investigate the performance of PB/N-doped CNTs/SPE and to find out the detection limit (Figs. S9A and B). The low detection limit that calculated by 3 times the signal to noise ratio was 0.26 μM for PB/N-doped CNTs/SPE. The sensitivity of the PB/N-doped CNTs/SPE is 0.52 μA μM^{-1} cm^{-2} based on the slope of the current-dose response curve and the surface area of the electrode. Furthermore, to explore the practical performance of PB/N-doped CNTs/SPE towards UA, different concentrations of UA were spiked into human serum without dilution. The analytical recovery was calculated by comparing the spiked and the strip-detected UA concentration. As shown in Fig. 4D, the recovery rates of PB/N-doped CNTs/SPE strip were in the range of 99–102%, indicating its practical application for analyzing UA in real biomedical samples. UA sensing performance of PB/N-doped CNTs was compared with that of previously reported works. As seen from the comparison results given in Table 1, the PB/N-doped CNTs offer a higher sensitivity and a lower detection limit, retaining its great potential for in-situ monitoring of UA. Specificity of the PB/N-doped CNTs/SPE for UA was studied with DA, AA, glucose, and H_2O_2 that usually coexist with UA as interfaces species in biological systems. Previously reported UA detections are based on electrochemical oxidation at a potential of around 0.25 V, which is close to that of the oxidation potentials of these interfaces species with a small difference in the range of 0.05–0.15 V, causing poor selectivity (Sheng et al., 2012). PB/N-doped CNTs/SPE can electrochemically catalyze UA in a reductive manner at a peak potential of around −0.5 V, at which insignificant responses are observed for the interfering species including DA, AA, glucose and H_2O_2 (Fig. 4E). In addition, the physiological concentration of the glucose (6 mM) was selected for the interference test in UA detection and other interferences tests were performed by using 0.2 mM, which are the maximum physiological concentrations in biological systems. In addition, the distance of oxygen atoms in AA, DA, H_2O_2, glucose is 2.452 Å,

Table 1
Comparison of various UA sensing platforms.

Sensing material	Analytical performance			Detection platform				Ref.
	Linear range [μM]	Sensitivity [μA μM^{-1} cm^{-2}]	Detection limit [μM]	Electrode	Non-enzymatic	Disposable strip	Detecting UA in serum	
PB/N-doped CNTs	1–1000	0.52	0.26	SPE	YES	YES	YES	This work
MoS_2 based flexible sensor	10–400	0.0983	1.169	Al foil	YES	NO	NO	Sha et al. (2019)
Pt@NP-AuSn/Ni	25–800	0.28	–	CFP	YES	NO	NO	Yang et al. (2019)
RGO/gold nanoparticle	25–200	–	5.4	SPE	YES	YES	NO	Ji et al. (2018)
PrGO/PB-100	40–415	–	8.0	GCE	YES	NO	NO	(dos Santos et al., 2018)

CFP: carbon fiber paper; PrGO: Photochemically reduced graphene oxide.

2.633 Å, 1.428 Å, 4.03 Å, respectively, which are not atomically matched with that (7.2 Å) of PB. Fig. S10 shows the poor selectivity of N-doped CNTs/SPE for these biomolecules.

3.4. Mechanical performance of the biomimetic UA strip

As a 1-D nanocomposite comprising CNTs and PB nanoparticles, PB/N-doped CNTs/SPE might be suitable as a soft material for flexible UA sensing. To investigate this possibility, the UA sensing performance of PB/N-doped CNTs/SPE under different bending angles and bending-release cycles was measured. Fig. S11A shows photographs of relaxing (a) and different bending angles (b: 30°, c: 90°, d: 120°) of the flexible platform, which can well retain its good mechanical integrity during bending. As shown in Fig. S11B, the current responses that were obtained for the sensing platform in 0.01 M PBS containing 1 mM UA remained 100% of its initial response after bending at 30°, and retained 93.2% after bending at 150°. The sensing platform was further subjected to bending-release cycles (Fig. S11C). After 200 bending-release cycles, it can still remain 81.7% of its initial response, demonstrating that PB/N-doped CNTs/SPE exhibits excellent mechanical stability for good flexibility.

3.5. Stability and reproducibility of the biomimetic UA strip sensor

Stability of the biomimetic reductive electrochemical strip was investigated by storage at room temperature (25 °C), and the UA sensing performance was measured per 7 days for a total period of 5 months (Fig. 4F). The biomimetic reductive electrochemical strip retained 98% of the initial response after 5 months, indicating an excellent stability. Fig. S12, demonstrates excellent stability of the UA sensor within 5 months. The excellent stability of PB/N-doped CNTs is contributed from its unique physicochemical properties. Particularly, PB nanoparticles were firmly embedded among sawtooth structure on the surface of N-doped CNTs, which enabled chemical and physical stability of PB nanoparticles to prevent their aggregation and leaching under reaction conditions. Finally, the reproducibility of both electrode fabrication and sensor measurement was investigated. The calculated reproducibility of the former is 98.6 ± 1.7%. Moreover, the measured reproducibility of the sensor is presented in Fig. S11D. This sensor could retain 85.4% of the initial response after 10 times of repeating tests, indicating a good reproducibility.

3.6. Catalytic mechanism for UA reduction on PB/N-doped CNT

Electrochemical reduction of UA on the PB/N-doped CNT was investigated by XPS (Fig. 5A and B). The results indicate that the C═O groups of UA decrease significantly after the reduction. On the other hand, there appears a new peak at 534.6 eV corresponding to C–OH, suggesting that C═O groups of UA molecules are reduced to be C–OH. It is observed that the reduction current of UA is much higher than the oxidation signal in comparison to the reported works. This is possibly resulted from the nitrogen doped-carbon substrate and the PB nanoparticles possessing much richer electrons for higher reduction ability. The catalytic mechanism of UA on PB/N-doped CNTs was proposed in Fig. 5C. Additionally, the *in-situ* deposited PB on N-doped CNTs have an average size as small as 10 nm, which is favorable in promoting high active catalytic site density, eventually leading to high sensitivity as observed.

4. Conclusion

In conclusion, an innovative biomimetic UA sensor comprising PB nanoparticles on N-doped CNTs was fabricated, and for the first time was used to sense UA with high selectivity and sensitivity. Investigation discovers that the distance between two reaction sites of UA matches well with that of the two Fe^{II} diagonally locating in PB lattice to realize an atomic matching catalysis for high selectivity and sensitivity toward UA reduction. The biomimetic UA sensor delivers an outstanding performance with a wide linear detection range (0.001–1 mM), a low detection limit (0.26 μM) and an excellent reproducibility. This work not only provides a unique biomimetic sensing platform for UA detection, but also presents an atomic matching catalysis approach, shedding a scientific light on fabrication of other highly selective and sensitive biomimetic sensors.

CRediT authorship contribution statement

Zhuanzhuan Shi: Conceptualization, Methodology, Data curation, Writing - original draft. **Xiaoli Li:** Conceptualization, Methodology. **Ling Yu:** Writing - review & editing. **Xiaoshuai Wu:** Visualization, Investigation. **Jinggao Wu:** Software, Validation. **Chunxian Guo:** Data curation, Validation, Writing - review & editing. **Chang Ming Li:** Writing - review & editing, Supervision.

Acknowledgement

This work is financially supported by National Natural Science Foundation of China (No. 31872753 and 21605110), Institute for Clean Energy & Advanced Materials (Southwest University, Chongqing, China), Chongqing Key Laboratory for Advanced Materials & Technologies of Clean Energies (Grant No. JJNY201903), Natural Science research Foundation of Jiangsu Higher Education Institutions and Natural Science Foundation of Suzhou University of Science and Technology. This work is also funded by Open Foundation of The Jiangsu Key Laboratory for Biochip and Medical diagnosis.

Appendix A. Supplementary data

Supplementary data to this article can be found online at https://doi.org/10.1016/j.bios.2019.111421.

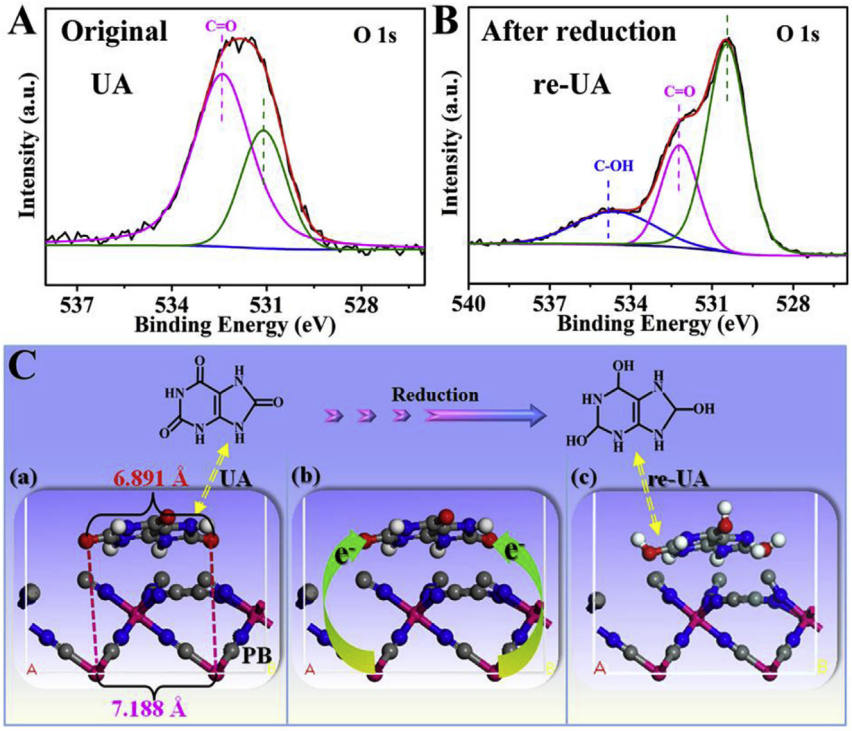

Fig. 5. O 1s spectra of UA before (A) and after reacted (B) with PB/N-doped CNTs. C. Electrocatalytic reaction mechanism of PB/N-doped CNTs/SPE-based UA strip: (a) adsorptions between the matched two Fe^{II} atoms and two oxygen atoms, (b) electron transfer, (c) obtaining re-UA.

Declaration of interests

☒The authors declare that they have no known competing financial interests or personal relationships that could have appeared to influence the work reported in this paper.

☐The authors declare the following financial interests/personal relationships which may be considered as potential competing interests

References

Bishop, C., Talbott, J.H., 1953. Pharmacol. Rev. 5 (3), 231–273.
Cao, L., Liu, Y., Zhang, B., Lu, L., 2010. ACS Appl. Mater. Interfaces 2 (8), 2339–2346.
Chen, L., Wang, X., Zhang, X., Zhang, H., 2012. J. Mater. Chem. 22 (41), 22090–22096.
Choi, B.G., Park, H., Park, T.J., Yang, M.H., Kim, J.S., Jang, S.-Y., Heo, N.S., Lee, S.Y., Kong, J., Hong, W.H., 2010. ACS Nano 4 (5), 2910–2918.
dos Santos, P.L., Katic, V., Toledo, K.C.F., Bonacin, J.A., 2018. Sensor. Actuator. B Chem. 255, 2437–2447.
Ghosh, T., Sarkar, P., Turner, A.P.F., 2015. Bioelectrochemistry 102, 1–9.
Guo, C.X., Ng, S.R., Khoo, S.Y., Zheng, X., Chen, P., Li, C.M., 2012. ACS Nano 6 (8), 6944–6951.
Guo, C.X., Zheng, X.T., Lu, Z.S., Lou, X.W., Li, C.M., 2010. Adv. Mater. 22 (45), 5164–5167.
Hu, F.X., Kang, Y.J., Du, F., Zhu, L., Xue, Y.H., Chen, T., Dai, L.M., Li, C.M., 2015. Adv. Funct. Mater. 25 (37), 5924–5932.
Ji, D., Liu, Z., Liu, L., Low, S.S., Lu, Y., Yu, X., Zhu, L., Li, C., Liu, Q., 2018. Biosens. Bioelectron. 119, 55–62.
Krstulovic, A.M., Brown, P.R., Rosie, D.M., 1977. Anal. Chem. 49 (14), 2237–2241.
Lang, X.-Y., Fu, H.-Y., Hou, C., Han, G.-F., Yang, P., Liu, Y.-B., Jiang, Q., 2013. Nat. Commun. 4, 2169.
Lee, S.-W., Lee, K.-Y., Song, Y.-W., Choi, W.K., Chang, J., Yi, H., 2016. Adv. Mater. 28 (8), 1577–1584.
Li, J., Xie, J., Gao, L., Li, C.M., 2015a. ACS Appl. Mater. Interfaces 7 (4), 2726–2734.
Li, L., Wang, Y., Pan, L., Shi, Y., Cheng, W., Shi, Y., Yu, G., 2015b. Nano Lett. 15 (2), 1146–1151.
Liao, C., Mak, C., Zhang, M., Chan, H.L.W., Yan, F., 2015. Adv. Mater. 27 (4), 676–681.
Liu, X., Qi, W., Wang, Y., Su, R., He, Z., 2017a. Nanoscale 9 (44), 17561–17570.
Liu, X., Zhang, Z., Zhang, Y., Guan, Y., Liu, Z., Ren, J., Qu, X., 2016. Adv. Funct. Mater. 26 (43), 7921–7928.
Liu, Y., Li, H., Guo, B., Wei, L., Chen, B., Zhang, Y., 2017b. Biosens. Bioelectron. 91, 734–740.
Ma, X., Hu, W., Guo, C., Yu, L., Gao, L., Xie, J., Li, C.M., 2014. Adv. Funct. Mater. 24 (37), 5897–5903.
Martinon, F., 2010. Immunol. Rev. 233, 218–232.
Noh, K.-G., Park, S.-Y., 2018. Adv. Funct. Mater. 28 (22), 1707562.
Sha, R., Vishnu, N., Badhulika, S., 2019. Sensor. Actuator. B Chem. 279, 53–60.
Sheng, Z.-H., Zheng, X.-Q., Xu, J.-Y., Bao, W.-J., Wang, F.-B., Xia, X.-H., 2012. Biosens. Bioelectron. 34 (1), 125–131.
Shi, Z., Wu, X., Lu, Y., Lu, Z., Li, C.M., Yu, L., 2018. Sensor. Actuator. B Chem. 255, 2431–2436.
Shi, Z., Wu, X., Zhang, H., Chai, H., Li, C.M., Lu, Z., Yu, L., 2019. J. Colloid Interface Sci. 534, 618–624.
Tian, J., Liu, Q., Cheng, N., Asiri, A.M., Sun, X., 2014. Angew. Chem. Int. Ed. 53 (36), 9577–9581.
Tiwari, J.N., Vij, V., Kemp, K.C., Kim, K.S., 2016. ACS Nano 10 (1), 46–80.
Wang, X., Sun, G., Routh, P., Kim, D.-H., Huang, W., Chen, P., 2014. Chem. Soc. Rev. 43 (20), 7067–7098.
Yang, H., Zhao, J., Qiu, M., Sun, P., Han, D., Niu, L., Cui, G., 2019. Biosens. Bioelectron. 124, 191–198.
Yu, J., Wang, S., Ge, L., Ge, S., 2011. Biosens. Bioelectron. 26 (7), 3284–3289.
Zhang, X.-Q., Gong, S.-W., Zhang, Y., Yang, T., Wang, C.-Y., Gu, N., 2010. J. Mater. Chem. 20 (24), 5110–5116.